SUPPLEMENTARY MATERIALS AND METHODS

Forewing morphology images

We required that each published forewing image considered for measurements met the following criteria: 1) contained a scale bar; 2) consisted of least one forewing zoomed out with all bristles shown; and 3) had no noticeable damage to any of the forewing bristles. For thrips, we used a different set of images for measurements of G and D, as we needed to substantially magnify each of these images (as compared to measurements of S_{max}, A_T and n). We required that the published forewing images considered for G and D measurements had a spatial resolution of at least 6 pixels per bristle diameter, similar to the criterion used by Jones et al. (2016). As G and D measurements were used to compute non-dimensional G/D ratios, we did not restrict the images selected for G and D measurements to only those that contained a scale bar (i.e. measurements of G and D in pixels sufficed to calculate the dimensionless G/D ratio). However, this resulted in mutually exclusive datasets in thrips for G/D versus the other variables (Appendix S1). We also note that we were unable to ensure bristle position or angle was unaffected during imaging. Thus, while we ensured that there was no visual damage to bristles, it is possible that the measurements of G were somewhat affected by the positioning uncertainty. High-magnification images of free-flying tiny insect wings are needed to address these two measurement uncertainties. Regardless, we expect this effect to be minor, as we measured G at the bristle root, where it attaches to the solid membrane. Rotation should be minimized at this location.

Phylogeny simulation details

We simulated phylogenies for our study taxa because very few of our study species have been sampled in published phylogenies. Of our 38 species of thrips with phenotypic data, only eight were in any one of the most comprehensive phylogenies published to date (Buckman et al., 2013; Lima and Mound, 2016; Pereyra et al., 2019). For fairyflies, the most comprehensive species-level phylogeny included only one of our 21 species (Munro et al., 2011). Moreover, no tree was ultrametric (i.e. all branches of extant species contemporaneous), which is optimal for phylogenetic comparative analyses (Butler and King, 2004; O'Meara, 2012). Thus, because most of our species could not be placed in phylogenies, we simulated many possible phylogenies for our study species and conducted regressions across these trees. This procedure allowed for both integration over phylogenetic uncertainty (Martins, 1996) and for assessment of the sensitivity of our results to any specific potential phylogeny (Losos, 1994). Moreover, we note that our regression analyses are likely to be robust to phylogenetic variation or inaccuracy for many reasons. First, the phylogenetic regression is generally robust to tree misspecification (Stone, 2011). Second, our use of lambda

should mitigate problems associated with contrasting phylogenetic and phenotypic structure in our data (e.g. phenotypically very different but closely related species, as in the same genus; Martins and Housworth 2002). Finally, ordinary least-squares regression (i.e. without phylogeny) and phylogenetic regression both give unbiased estimates of the interspecific regression slope (Pagel, 1993; Rohlf, 2006), our focus here.

Adding some phylogenetic structure to simulated trees, rather than using completely random approaches, increases accuracy in downstream comparative analyses (Housworth and Martins, 2001; Martins, 1996; Martins and Housworth, 2002; Symonds, 2002). Thus, we ensured the simulated trees fit best estimates of taxonomy, given that taxonomy in principle reflects estimates of evolutionary relationships. At the lowest taxonomic level, all species of given genus were each other's closest relatives in every simulated tree. By adding additional taxonomic structure (i.e. subfamilies, families, suborders), our simulated trees were similarly constrained to best represent estimated relationships among higher taxa (Buckman et al., 2013).

For thrips, we first extracted taxonomic information from the Thrips Wiki (https://thrips.info/wiki/; accessed 15 March 2021). This source is updated regularly by researchers studying thrips systematics and is consistent with the current best estimate of higher-level thrips phylogeny (Buckman et al., 2013). Data were extracted on genera within families and families within the two major sub-orders of thrips (Terebrantia and Tubulifera). In some cases genera were placed into subfamilies, which were placed in families. All genera were included, including extinct genera and those unrepresented in our phenotypic data, to best simulate the branch-length structure among groups (e.g. mean genus age in a family of 100 genera will be lower than mean genus age in an equally old family of two genera). Current estimates of wasp systematics suggest that fairyflies are a polyphyletic group of two families in two superfamilies of wasps (Mymarommatoidea: Mymarommatidae and Chalcidoidea: Myrmaridae; Huber 1986; Davis et al. 2010; Munro et al. 2011). However, the two superfamilies may be sister clades, and Mymaridae is the sister family to all other clades within Chalcidoidea (Heraty et al., 2013; Munro et al., 2011). Thus, additional taxonomic structure would not have greatly improved our simulated trees. So for analysis purposes, we assumed these two families to be each other's sister taxon. We compiled genera for these two families from taxonomic accounts (Gibson et al., 2007; Huber, 2005, 2017; Lin et al., 2007; Poinar and Huber, 2011).

We simulated phylogenies in the package *phytools* v.0.7-70 (Revell, 2012) in R v.4.0.2 (R Core Team 2020). Because thrips and fairyflies are so distantly related phylogenetically (separated for more than 350 million years; Johnson et al., 2018; Misof et al., 2014), we started each simulated tree with these two groups as sister clades using the function "pbsim". We then simulated structure at sequentially lower taxonomic levels using the function "genus.to.species". These two functions simulated both tree topology and branch lengths. For both fairyflies and thrips, multiple levels of taxonomic ranks were imposed in simulations. In thrips, this meant randomly placing the branching time of the two suborders within Thysanoptera, then families within those suborders, subfamilies within some families, genera within (sub)families, and species within genera. For fairyflies, families were placed within superfamilies, genera within families, and species within genera.

We simulated 10,000 trees for our analyses. To remove variation in tree length due to stochastic simulation variation (Stadler, 2011), each simulated tree was rescaled to a total length of 1.0. Note that the relative (not absolute) amount of shared history between any two species determines the effect of phylogeny in PGLS (Hansen and Martins, 1996; Martins and Hansen, 1997). Thus our choice of 1.0 for tree length was arbitrary and did not affect our results. After simulation, each tree was pruned to only include the species for which we had phenotypic data, which varied based on the response variable (see above). We provide all tree simulation R code, taxonomic information, and resulting trees in Figshare as Appendices S2–4.

Bristled wing fabrication

The 3 mm thick solid membrane used in all the wing models were 3D printed with polylactic acid (PLA) filament using Craftbot printers (CraftUnique LLC, Stillwater, OK, USA). The bristles were made of type 304 stainless steel wires of varying diameter (Table S1), glued on top of the membrane. For flow-visualization measurements using particle image velocimetry (PIV), we made new wing models with the solid membrane laser cut from 3 mm thick acrylic sheets. Also, to avoid reflection in PIV measurements, the bristles were blackened using a blackener kit (Insta-Blak SS-370, Electrochemical Products, Inc., New Berlin, WI, USA).

Dynamically scaled robotic platform

Bristled wing models were attached to 6.35 mm diameter stainless steel D-shafts via custom aluminum L-brackets. Two 2-phase hybrid stepper motors with integrated encoders (ST234E, National Instruments Corporation, Austin, TX, USA) were used on each wing to perform rotation and translation. Rotational motion on a wing was achieved using a bevel gear for coupling a motor to a D-shaft. Translational motion was achieved using a rack and pinion mechanism driven by a second

motor. All four stepper motors (for a wing pair) were controlled using a multi-axis controller (PCI-7350, National Instruments Corporation, Austin, TX, USA) via custom programs written in LabVIEW software (National Instruments Corporation, Austin, TX, USA). The assembly was mounted on an acrylic tank measuring 0.51 m x 0.51 m in cross-section, and 0.41 m in height. The tank was filled to 0.31 m in height with a 99% glycerin solution, such that the wings were completely immersed in the fluid medium. This solution allowed us to achieve fluid properties relevant to tiny insect flight at a robot size large enough to accurately adjust the relevant parameters (see the **Test conditions** subsection in the main article).

Justification of forewing approach

Many miniaturized tiny insects possess hindwings as well as forewings (Jones et al., 2016, Santhanakrishnan et al., 2014, Kasoju et al., 2018, Cheng & Sun 2018, Lyu et al., 2019). From high-speed video recording of thrips (Santhanakrishnan et al., 2014, Cheng & Sun 2018, Lyu et al., 2019), it appears that there is a phase-lag between hind- and forewings during dorsal and ventral stroke reversal. As per our knowledge, wingbeat kinematics of hindwings of tiny insects have not been previously examined. In addition, a separate study would be required to understand the aerodynamic effects of including a phase lag between hind wings and fore wings. However, since these insects are flapping both hind wings and fore wings synchronously for most of the flapping cycle (except during dorsal and ventral stroke reversal), we expect that results for the forewing can be extended to the hindwing. Considering the above criteria, modelling just the forewing should be sufficient to understand the aerodynamic characteristics of bristled wing morphology. However, we recognize that this may be a fruitful area for future work.

Inter-wing spacing

The wing separation maintained in this study is similar to those observed in high-speed video recordings of free-flying thrips (Santhanakrishnan et al., 2014) and is also close enough to experience wing-wing interactions, but just far enough apart to prevent the leading and trailing edges of the rigid wing models from colliding during rotation. The variation in wing separation at the end of clap and start of fling is considered in our recent study (Kasoju and Santhanakrishnan, 2021), where we found that our smallest tested gap of 10% chord length between the wings augmented the aerodynamic force generation significantly. This occurred because the pressure distribution varied in the gap between the wings. Due to design limitations of our test facility, we were unable to test the case where the opposing wings come in full contact. More generally, if most species deviate the same way from our models, our results will apply equally to all of them. In other words, while our force measurements may underestimate the actual magnitudes, such an underestimation should

equally apply to all species, and thus our results on the effects of different variables (e.g. wingspan, bristle number, G, D) should be robust to this assumption.

Force measurements

A pause of 30 sec was introduced at the end of each run to remove the influence of wing-wake interaction occurring from the stroke reversal between runs. Another reason for introducing pause between runs is to remove any mechanical disturbance between runs (e.g. sudden bending of the L-bracket when the wings come to rest quickly). However, before commencing multiple runs for data collection (forces, TR-PIV, PL-PIV measurements), we operated the setup for at least 10 runs (without pausing between runs) to establish a periodic steady state in the tank. Operating for at least 10 runs before any data collection has been our standard protocol (Kasoju et al., 2018, Ford et al., 2019, Kasoju & Santhanakrishnan, 2021) to avoid any disturbances (such as sudden motion in a quiescent fluid) in data collection from the first run to the last run of data collection, and we favor it because this procedure helps us build a similar fluid environment for each run of data collection. In previous studies, this protocol was found to be helpful in maintaining repeatable force data collection between runs at high Reynolds number flows (Re_c>100). However, at a lower Reynolds number as in this study (Re_c=10), we did not see any noticeable difference from run to run with or without this protocol, since we were waiting for 30 seconds between run to run.

2D flow validation

Our assumption of 2D flow simplification is valid for two key reasons. First, in our previous study (Kasoju et al., 2018), we observed no flow along the z-direction of a rectangular bristled wing model. Second, in our more recent study (Kasoju & Santhanakrishnan, 2021), we found a very small region of non-zero 2D divergence in the flow field, suggesting that 2D flow simplification is a reasonable approximation. Our 2D flow simplification is also in agreement with a recent study (Santhanakrishnan et al., 2018) of a revolving elliptical wing of similar aspect ratio (~2) as this study, where spanwise flow was reduced for Re_c<10.

2D TR-PIV along wing chord

2D TR-PIV measurements were acquired for a total of 6 wing pairs, consisting of 2 wing pairs each for varying G, D and S. TR-PIV measurements were acquired along a chordwise (i.e. x-y) plane located at mid-span (Fig. 3A). The TR-PIV experimental setup and processing were similar to our previous studies (Kasoju et al., 2018; Ford et al., 2019) and are briefly summarized here. A single cavity Nd:YLF laser (Photonics Industries International, Inc., Bohemia, NY, USA) that provided a 0.5 mm diameter beam of 527 nm in wavelength was used in combination with a plano-concave cylindrical lens (focal length=-10 mm) to generate a thin laser sheet (thickness≈3-5 mm) positioned

at mid-span (HP in Fig. 3A) to illuminate the field of view (FOV). TR-PIV images were acquired using a high-speed complementary metal-oxide-semiconductor (CMOS) camera with a spatial resolution of 1280 x 800 pixels, maximum frame rate of 1630 frames/s, and pixel size of 20 x 20 microns (Phantom Miro 110, Vision Research Inc., Wayne, NJ, USA). This camera was fitted with a 60 mm lens (Nikon Micro Nikkor, Nikon Corporation, Tokyo, Japan). Hollow glass spheres of 10-micron diameter (110P8, LaVision GmbH, Göttingen, Germany) were used as seeding particles. A frame rate of 90 Hz was used to capture 100 evenly spaced images during both clap and fling phases. The raw images were processed using DaVis 8.3.0 software (LaVision GmbH, Göttingen, Germany) using one pass with an interrogation window of 64x64 pixels and two subsequent passes of 32x32 pixels window size.

2D PL-PIV along wingspan

The PL-PIV setup was similar to that used in Kasoju et al. (2018) and is briefly described here. Illumination was provided using a double-pulsed Nd:YAG laser (Gemini 200-15, New Wave Research, Fremont, CA) with a wavelength of 532 nm, maximum repetition rate of 15 Hz, and pulse width in the range of 3–5 ns. A 10 mm focal length cylindrical lens was used to generate a thin laser sheet (thickness≈3-5 mm) for illuminating the FOV. Raw PL-PIV images were acquired using a scientific CMOS (sCMOS) camera with a maximum spatial resolution of 2600 x 2200 pixels (maximum pixel size=6.5 x 6.5 microns) at a frame rate of 50 frames/s (LaVision Inc.,Ypsilanti, MI, USA), mounted with a 60 mm lens (same lens as in TR-PIV). The camera was focused on the seeding particles (same particles as in TR-PIV) along the laser sheet. PL-PIV measurements were acquired for all the wing models along 2 spanwise planes (VP1: fling and VP2: clap; see Fig. 3C) located at $0.5L_b$ measured from the membrane. Raw image pairs were acquired at 6 time points in clap and 7 time points in fling, with adjacent time points spaced by 6.25% τ. Laser pulse separation intervals between the 2 images of an image pair ranged from 1,500 -19,831 μs to obtain 6-8 pixels of particle displacement. The starting time point during the clap phase (τ=0.0625) was neglected due to very small changes in flow surrounding the wings. For each wing model tested, 5 image pairs were acquired at each time point for 5 continuous cycles of clap and fling. The raw image pairs were processed using DaVis 8.3.0 using one pass with an interrogation window of 64 x 64 pixels and two subsequent passes of 32 x 32 pixels window size. The processed PL-PIV images were phase-averaged over 5 cycles and the velocity field was exported to quantify the amount of fluid leaked through the bristles along the wingspan.

Circulation calculation

For a particular test condition (individually varying *G*, *D*, and *S*), the maximum absolute values of ω_z (i.e., $|\omega_z|$) at both LEV and TEV of a bristled wing were identified. Similar to Ford et al. (2019) and

Kasoju & Santhanakrishnan (2021), a 10%$|\omega_z|$ high-pass cut-off was next applied to isolate the vortex cores on a bristled wing model for that test condition. Γ of LEV or TEV was then calculated by selecting a region of interest (ROI) by drawing a box around a vortex core. A custom MATLAB script was used to automate the process of determining the ROI (Samaee et al. 2020). Essentially, we iterated the selection of ROI by starting with a small square box of 2 mm edge length and compared the Γ value with that of a bigger square box of 5 mm edge length. If the circulation values matched between the 2 boxes, then we stopped further iteration. If the circulation values did not match between the 2 boxes, we increased the size of the smaller box by 3 mm and repeated the process. In order to work with a single vortex (LEV or TEV) at a time and to remove any bias of Γ estimation, we ensured that ω_z of the oppositely signed vortex was zeroed out. Γ was determined for the right-hand wing only, with the assumption that circulation for the left wing was equivalent in magnitude but oppositely signed. Note that the left-wing motion is symmetric to the right wing about the *y-z* plane, making our assumption justifiable.

REFERENCES

Buckman, R. S., Mound, L. A. and Whiting, M. F. (2013). Phylogeny of thrips (Insecta: Thysanoptera) based on five molecular loci. *Syst. Entomol.* **38**, 123–133. doi:10.1111/j.1365-3113.2012.00650.x

Burnham, K. P. and Anderson, D. R. (2002). Model selection and multimodel inference: a practical information-theoretic approach. New York, NY: Springer-Verlag.

Butler, M. A. and King, A. A. (2004). Phylogenetic comparative analysis: a modeling approach for adaptive evolution. *Am. Nat.* **164**, 683–695. doi:10.1086/426002

Cheng, X., & Sun, M. (2018). Very small insects use novel wing flapping and drag principle to generate the weight-supporting vertical force. *J. Fluid Mech. 855*, 646-670. doi:10.1017/jfm.2018.668.

Davis, R. B., Baldauf, S. L. and Mayhew, P. J. (2010). The origins of species richness in the Hymenoptera: insights from a family-level supertree. *BMC Evol. Biol.* **10**, 109. http://www.biomedcentral.com/1471-2148/10/109.

Ford, M. P., Kasoju, V. T., Gaddam, M. G. and Santhanakrishnan, A. (2019). Aerodynamic effects of varying solid surface area of bristled wings performing clap and fling. *Bioinspir. Biomim.* **14**, 046003. doi:10.1088/1748-3190/ab1a00.

Gibson, G. A. P., Read, J. and Huber, J. T. (2007). Diversity, classification and higher relationships of Mymarommatoidea (Hymenoptera). *J. Hymenoptera Res.* **16**, 51–146.

Hansen, T. F. and Martins, E. P. (1996). Translating between microevolutionary process and macroevolutionary patterns: the correlation structure of interspecific data. *Evolution* **50**, 1404–1417.

Heraty, J. M., Burks, R. A., Cruaud, A., Gibson, G. A. P., Liljeblad, J., Munro, J., Rasplus, J. Y., Delvare, G., Jansta, P., Gumovsky, A. et al. (2013). A phylogenetic analysis of the megadiverse Chalcidoidea (Hymenoptera). *Cladistics* **29**, 466–542. doi:10.1111/cla.12006

Housworth, E. A. and Martins, E. P. (2001). Random sampling of constrained phylogenies: conducting phylogenetic analyses when the phylogeny is partially known. *Syst. Biol.* **50**, 628–639.

Huber, J. T. (1986). Systematics, biology, and hosts of the Mymaridae and Mymarommatidae (Insecta: Hymenoptera). *Entomography* **4**, 185–243.

Huber, J. T. (2005). The gender and derivation of genus-group names in Mymaridae and Mymarommatidae (Hymenoptera). *Acta Soc. Zool. Bohem.* **69**, 167–183.

Huber, J. T. (2017). *Eustochomorpha* Girault, *Neotriadomerus* gen. n., and *Proarescon* gen. n. (Hymenoptera, Mymaridae), early extant lineages in evolution of the family. *Journal of Hymenoptera Research* **57**, 1–87. doi:10.3897/jhr.57.12892

Johnson, K. P., Dietrich, C. H., Friedrich, F., Beutel, R. G., Wipfler, B., Peters, R. S., Allen, J. M., Petersen, M., Donath, A., Walden, K. K. O. et al. (2018). Phylogenomics and the evolution of hemipteroid insects. *Proc. Natl. Acad. Sci. USA* **115**, 12775–12780. doi:10.1073/pnas.1815820115

Jones, S. K., Yun, Y. J. J., Hedrick, T. L., Griffith, B. E. and Miller, L. A. (2016). Bristles reduce the force required to 'fling' wings apart in the smallest insects. *J. Exp. Biol.* **219**, 3759–3772. doi:10.1242/jeb.143362.

Kasoju, V. T., & Santhanakrishnan, A. (2021). Aerodynamic interaction of bristled wing pairs in fling. *Phys. Fluids*, *33*(3), 031901.

Kasoju, V. T., Terrill, C. L., Ford, M. P. and Santhanakrishnan, A. (2018). Leaky flow through simplified physical models of bristled wings of tiny insects during clap and fling. *Fluids* **3**, 44. doi:10.3390/fluids3020044.

Lima, É. F. B. and Mound, L. A. (2016). Systematic relationships of the Thripidae subfamily Sericothripinae (Insecta: Thysanoptera). *Zool. Anz.* **263**, 24–32. doi:10.1016/j.jcz.2016.03.001

Lin, N. Q., Huber, J. T. and LaSalle, J. (2007). The Australian genera of Mymaridae (Hymenoptera: Chalcidoidea). *Zootaxa* **1596**, 1–111. doi:10.11646/zootaxa.1596.1.1

Losos, J. B. (1994). An approach to the analysis of comparative data when a phylogeny is unavailable or incomplete. *Syst. Biol.* **43**, 117–123.

Lyu, Y. Z., Zhu, H. J., & Sun, M. (2019). Flapping-mode changes and aerodynamic mechanisms in miniature insects. *Physical Rev. E*, **99**(1-1), 012419. doi:10.1103/PhysRevE.99.012419.

Martins, E. P. (1996). Conducting phylogenetic comparative studies when the phylogeny is not known. *Evolution* **50**, 12–22.

Martins, E. P. and Hansen, T. F. (1997). Phylogenies and the comparative method: a general approach to incorporating phylogenetic information into the analysis of interspecific data. *Am. Nat.* **149**, 646–667.

Martins, E. P. and Housworth, E. A. (2002). Phylogeny shape and the phylogenetic comparative method. *Syst. Biol.* **51**, 873–880. doi:10.1080/10635150290155863

Misof, B. Liu, S. Meusemann, K. Peters, R. S. Donath, A. Mayer, C. Frandsen, P. B. Ware, J. Flouri, T. Beutel, R. G. et al. (2014). Phylogenomics resolves the timing and pattern of insect evolution. *Science* **346**, 763–767. doi:10.1126/science.1257570

Munro, J. B., Heraty, J. M., Burks, R. A., Hawks, D., Mottern, J., Cruaud, A., Rasplus, J. Y. and Jansta, P. (2011). A molecular phylogeny of the Chalcidoidea (Hymenoptera). *PLoS One* **6**, e27023. doi:10.1371/journal.pone.0027023

O'Meara, B. C. (2012). Evolutionary inferences from phylogenies: a review of methods. *Annu. Rev. Ecol. Evol. Syst.* **43**, 267–285. doi:10.1146/annurev-ecolsys-110411-160331

Pagel, M. (1993). Seeking the evolutionary regression coefficient: an analysis of what comparative methods measure. *J. Theoret. Biol.* **164**, 191-205.

Pereyra, V., Cavalleri, A., Szumik, C. and Weirauch, C. (2019). Phylogenetic analysis of the New World family Heterothripidae (Thysanoptera, Terebrantia) based on morphological and molecular evidence. *Insect Syst. Evol.* **50**, 702–716. doi:10.1163/1876312x-00002193

Poinar, G., Jr. and Huber, J. T. (2011). A new genus of fossil Mymaridae (Hymenoptera) from Cretaceous amber and key to Cretaceous mymarid genera. *Zookeys*, 461–472. doi:10.3897/zookeys.130.1241

R Core Team (2020). R: a language and environment for statistical computing. Vienna: R Foundation for Statistical Computing.

Revell, L. J. (2012). phytools: an R package for phylogenetic comparative biology (and other things). *Methods Ecol. Evol.* **3**, 217–223. doi:10.1111/j.2041-210X.2011.00169.x

Rohlf, F. J. (2006). A comment on phylogenetic correction. *Evolution* **60**, 1509–1515.

Samaee, M., Nelsen, N. H., Gaddam, M. G., & Santhanakrishnan, A. (2020). Diastolic vortex alterations with reducing left ventricular volume: an in vitro study. *J. Biomech. Eng.*, **142**(12), 121006. doi:10.1115/1.4047663.

Santhanakrishnan, A., Robinson, A. K., Jones, S., Low, A. A., Gadi, S., Hedrick, T. L. and Miller, L. A. (2014). Clap and fling mechanism with interacting porous wings in tiny insects. *J. Exp. Biol.* **217**, 3898–3909. doi:10.1242/jeb.084897.

Sokal, R. R. and Rohlf, F. J. (1995). *Biometry*. New York, NY: W.H. Freeman.

Stadler, T. (2011). Simulating trees with a fixed number of extant species. *Syst. Biol.* **60**, 676–684. doi:10.1093/sysbio/syr029

Stone, E. A. (2011). Why the phylogenetic regression appears robust to tree misspecification. *Syst. Biol.* **60**, 245–260. doi:10.1093/sysbio/syq098

Symonds, M. R. (2002). The effects of topological inaccuracy in evolutionary trees on the phylogenetic comparative method of independent contrasts. *Syst. Biol.* **51**, 541–553. doi:10.1080/10635150290069977
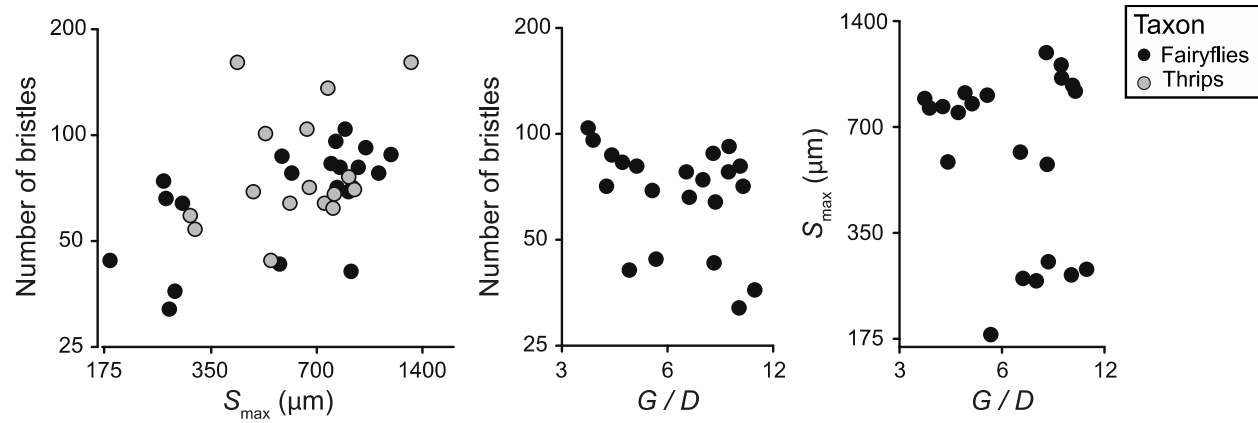
Fig. S1. Scatter plots of wing variables measured across thrips and fairyflies. All variables are plotted in raw units on a logged scale. Fairyfly data across all plots are from the same species. Thrips species measured for S_{max} and number of bristles (n) were different species than those for which we measured G/D, preventing plotting and correlation among those variables. All correlations among wing variables were low and statistically insignificant (Table S3).

Table S1. Experimental conditions and physical wing models used in this study. Each row represents the specific geometric variable or ratio that was controllably changed. Wing chord (c)=45 mm, membrane width (w)=7 mm, and bristle length (L_b)=19 mm were maintained constant across all wing models. G, D, S and n represent inter-bristle gap, bristle diameter, wingspan and number of bristles, respectively. 23 pairs of physical wing models were tested in this study. 3 wing pairs included in the case of varying n overlapped with 3 of the wing pairs considered in varying D, varying S and varying G/D conditions.

Experiment	Number of wing pairs tested	S [mm]	G [mm]	D [mm]	n	G/D
Changing G	4	81	1 – 2.1	0.2	70 – 132	5 – 10
Changing D	5	81	1.4	0.13 – 0.64	78 – 106	2 – 11
Changing S	5	67.5 – 94.5	1.3 – 1.8	0.25 – 0.36	88	5
Changing n	8	81	1 – 19	0.2 – 3.81	6 – 132	5
Changing G/D	4	81	1.2 – 1.8	0.15 – 0.6	88	2 – 11

Table S2. Results of regression model fitting of wing variables on body length in thrips and fairyflies. Models were fit separately for each variable. "Model" refers to parameter independence in thrips and fairyflies; the null model only contained a shared intercept and no slope, whereas the full model allowed a different slope and intercept for both groups. Each numerical value in the table is the mean across simulated phylogenies. AICc is the small-sample Akaike Information Criterion; low value indicates highest statistical support. w_i is the AICc weight, the probability that each model is the optimal model relative to the others (Burnham and Anderson 2002). Rank indicates the mean model rank across phylogenies, with 1 indicating the top model and 4 the poorest fit.

Model	Span (S_{max})			Bristle number			G/D		
	AICc	w_i	Rank	AICc	w_i	Rank	AICc	w_i	Rank
Null (same intercept, no slope)	50.95	0.000	4.000	33.93	0.001	4.000	46.26	0.000	4.000
Same slope + intercept	12.23	0.610	1.120	21.75	0.447	1.474	32.60	0.370	1.559
Same slope, different intercept	13.69	0.306	1.889	21.74	0.444	1.526	34.93	0.119	2.984
Full (slope + intercept different)	16.30	0.084	2.992	24.57	0.108	3.000	31.94	0.510	1.458

Table S3. PGLS correlations among wing variables. The correlation between S_{max} and n includes data from thrips and fairyflies. Correlations between S_{max} and G/D, as well as n and G/D, only included fairyflies, as thrips datasets for G/D versus n and S_{max} were mutually exclusive (Appendix S1). Correlations are on the lower diagonal (unshaded) and represent mean values across simulated phylogenies, corrected for bias (Rohlf 2006). *P*-values are on the upper diagonal (shaded) and likewise represent mean values across simulated phylogenies. *P*-values were calculated using Z-scores (Sokal and Rohlf, 1995).
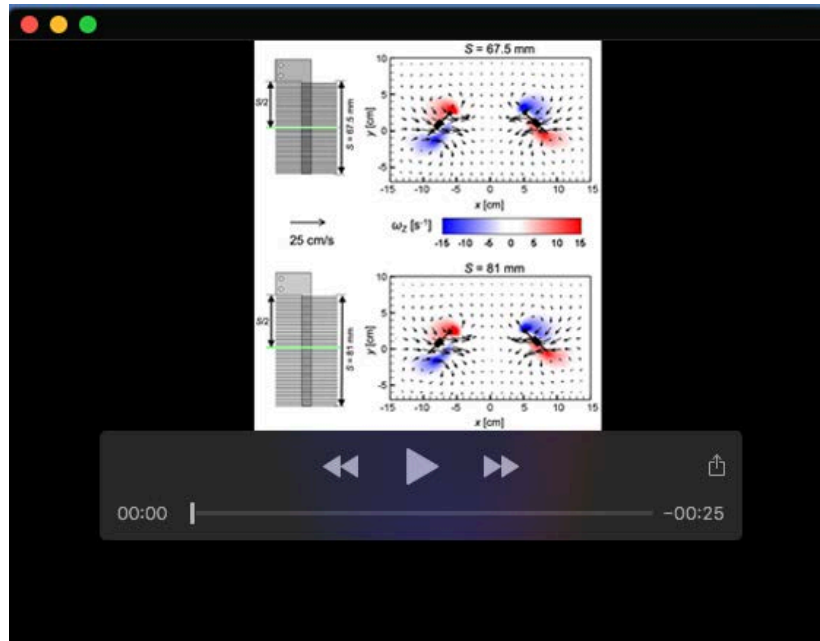
	S_{max}	n	G/D
S_{max}	-	0.078	0.211
n	0.431	-	0.133
G/D	-0.378	-0.511	-
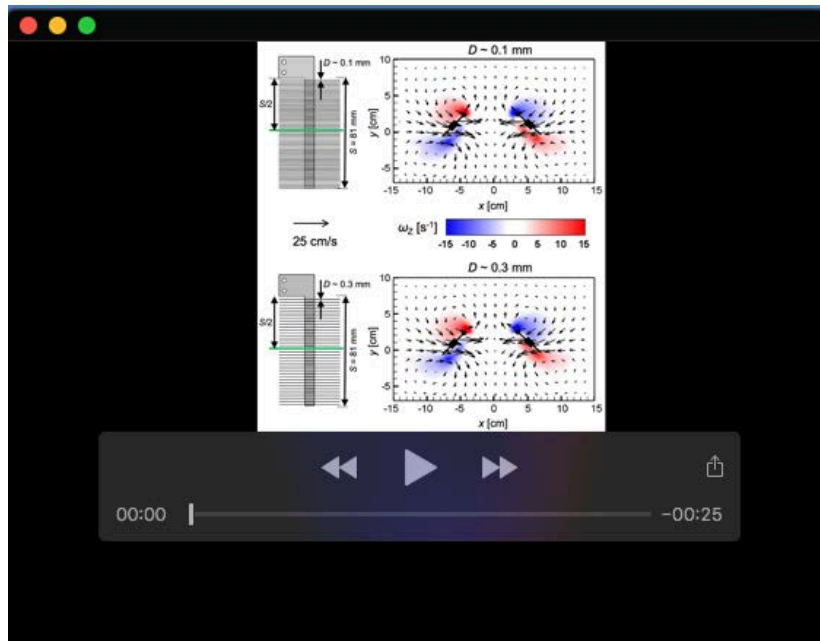
Movie 1. Velocity vectors overlaid on out-of-plane vorticity (ω_z) contours of bristled wing pairs during clap and fling, comparing the effect of increasing bristle diameter (*D*) from 0.1 mm to 0.3 mm. 10 equally spaced time instances are shown from start to end of clap, followed by 8 equally spaced time instances during fling.
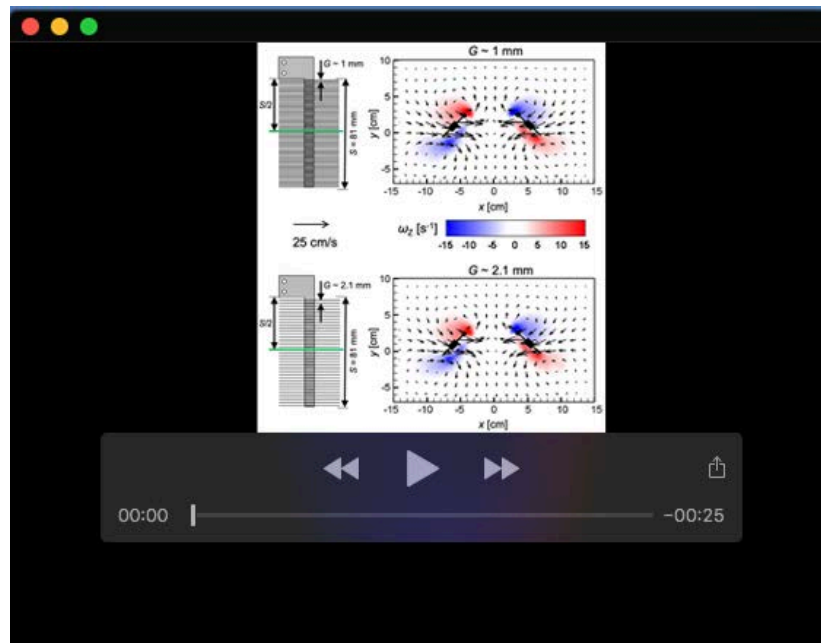
Movie 2. Velocity vectors overlaid on out-of-plane vorticity (ω_z) contours of bristled wing pairs during clap and fling, comparing the effect of increasing inter-bristle gap (*G*) from 1 mm to 2.1 mm. 10 equally spaced time instances are shown from start to end of clap, followed by 8 equally spaced time instances during fling.

Movie 3. Velocity vectors overlaid on out-of-plane vorticity (ω_z) contours of bristled wing pairs during clap and fling, comparing the effect of increasing wingspan (S) from 67.5 mm to 81 mm. 10 equally spaced time instances are shown from start to end of clap, followed by 8 equally spaced time instances during fling.